Research Article Vol. 12, No. 9 / 1 Sep 2021 / *Biomedical Optics Express* 5812

Biomedical Optics EXPRESS

Disassembly of microtubules by intense terahertz pulses

CAMERON M. HOUGH,[1,2,*] DAVID N. PURSCHKE,[2] CLAYTON BELL,[1] AARAT P. KALRA,[1,3] PATRICIA J. OLIVA,[2] CHENXI HUANG,[2] JACK A. TUSZYNSKI,[1,2] BRAD J. WARKENTIN,[1] AND FRANK A. HEGMANN[2]

[1] *Department of Oncology, University of Alberta, Edmonton, AB T6G 2E1, Canada*
[2] *Department of Physics, University of Alberta, Edmonton, AB T6G 2E1, Canada*
[3] *Currently with the Department of Chemistry, Frick Chemistry Laboratory, Princeton University, Princeton, NJ 08540, USA*
[*] *chough@ualberta.ca*

Abstract: The biological effects of terahertz (THz) radiation have been observed across multiple levels of biological organization, however the sub-cellular mechanisms underlying the phenotypic changes remain to be elucidated. Filamentous protein complexes such as microtubules are essential cytoskeletal structures that regulate diverse biological functions, and these may be an important target for THz interactions underlying THz-induced effects observed at the cellular or tissue level. Here, we show disassembly of microtubules within minutes of exposure to extended trains of intense, picosecond-duration THz pulses. Further, the rate of disassembly depends on THz intensity and spectral content. As inhibition of microtubule dynamics is a mechanism of clinically-utilized anti-cancer agents, disruption of microtubule networks may indicate a potential therapeutic mechanism of intense THz pulses.

© 2021 Optical Society of America under the terms of the OSA Open Access Publishing Agreement

1. Introduction

In animal cells, the cytoskeleton is a cytoplasmic network of interlinking filamentous protein polymers of three main types: intermediate filaments, actin, and microtubules (MTs) [1,2]. These complexes form a dynamic structure that connects the cell physically and biochemically to the extracellular environment, facilitates chemical transport, provides mechanical stability, and regulates morphology, intracellular traffic, and motility. MTs are the most mechanically rigid of the cytoskeletal polymers, and form the dominant component of the mitotic spindle, providing the structural framework and force-generation necessary to carry out mitosis [1]. General MT function depends strongly on a dynamic instability between states of polymerization and rapid depolymerization [2,3].

MTs are comprised of tubulin dimer subunits, which are themselves a complex of bound α and β tubulin proteins, as shown in Fig. 1(a). Structurally, $\alpha\beta$-tubulin dimers spontaneously polymerize to form thirteen 1D protofilaments that bind laterally to form polar cylindrical MTs; they depolymerize via GTP (guanosine tri-phosphate) hydrolysis of tubulin dimers on the positive end [4]. Importantly, dimers and protofilaments bind via hydrogen-bonding, for which the natural oscillatory frequencies occupy a broad region of the THz band (0.1–10 THz) [5–7]. External excitation of MTs with intense THz pulses may efficiently couple to these oscillations and dysregulate structural dynamics, which may in turn affect important MT functions such as polymerization and de-polymerization.

Since THz radiation is non-ionizing, it is typically regarded as a non-destructive probe of hydration level, biomolecular structure, or chemical concentration, and has been applied in clinical applications for diagnostic spectroscopy or imaging [9–14]. However, THz radiation has

#433240 https://doi.org/10.1364/BOE.433240
Journal © 2021 Received 9 Jun 2021; revised 12 Aug 2021; accepted 12 Aug 2021; published 24 Aug 2021

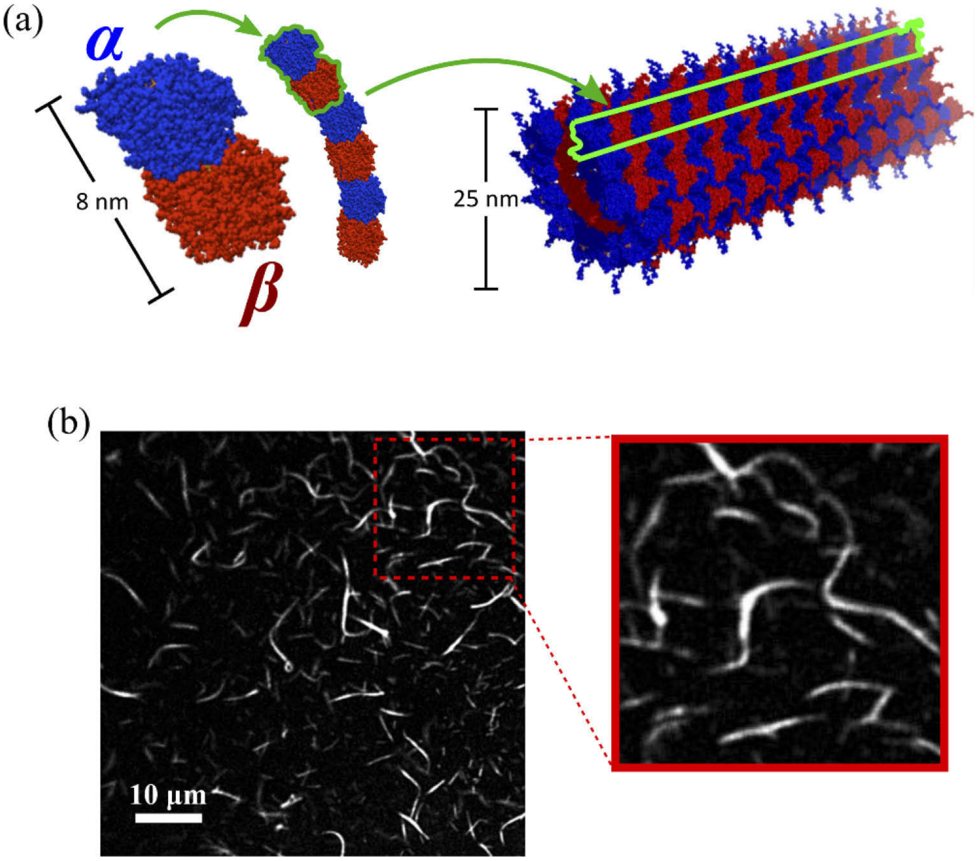

Fig. 1. Microtubule structure and fluorescence microscopy image. (a) Bound $\alpha\beta$-tubulin dimers comprise the hydrogen-bonded protofilaments [8]. 13 protofilaments laterally bind to form a hollow cylindrical polymer with a 25 nm diameter. Green outlines indicate a tubulin dimer that comprises a protofilament, and a single protofilament that comprises the polymerized MT. (b) Fluorescence image of rhodamine-labelled polymerized microtubules in solution, with an average length of 10 µm. The inset shows a zoomed window of polymerized MTs in a 20 µm square window.

been observed to induce significant effects at multiple levels of biological organization that are not explained by the estimated heating [15–18]. While the specific nature of the fundamental interactions is not yet understood, these phenotypic effects may be attributable to interaction with sub-cellular macromolecular structures such as DNA [19–22] or cellular membranes [23–25]. However, experimental investigation of THz exposure effects to cytoskeletal protein complexes is still at a preliminary stage. Studies by Yamazaki et al. show that THz exposures of relatively low intensity (~0.6 W/cm^2) can stimulate polymerization of actin, while highly intense THz pulses (~3 GW/cm^2) resulted in actin disassembly [26,27]. To date, no studies have directly investigated the structural changes to MTs irradiated by intense THz pulses, although there have been indications in the literature that this may be an important interaction mechanism [28–31]. Hintzche et al. observed disturbance to the spindle apparatus (a mitotic structure comprised of microtubules) in hybrid animal cells [28], and Amicis et al. observed significant increase of micronuclei in THz-exposed human epithelial cells, which arise due to abnormal mitotic activity forming multiple nuclear envelopes in non-viable daughter cells [29].

Simulation studies investigating MT structure in nanosecond-duration pulsed electric fields have been reported, and show significant structural dysregulation for field strengths in the range of 50–750 kV/cm [32–34]. These studies predict reduction of MT stability proportional to field strength through conformational changes to key loops involved in lateral protofilament contact (Fig. 1(a)), or alteration of local electrostatic properties at the GTP binding site. These results theoretically motivate the hypothesis that intense picosecond-duration pulses may also induce similar field-induced structural effects; however, more work simulating tubulin/MT response specifically to intense picosecond-duration fields is necessary. Simulation studies of THz fields for other macromolecular structures, such as membranes, offer insight into the expected interaction with intracellular environments [23]. For long-duration pulses (>∼10 ns), membrane interactions are predominantly due to ionic redistribution, as the field variations allow sufficient time for these motions to occur [35,36]. In contrast, for fast, short-duration pulses (<∼1 ns), the interaction is predominantly dielectric, arising from faster dipole reorientation dynamics. Importantly, this suggests that picosecond-duration pulses with sufficient field strength may interact with interior cellular structures, since the electronic screening effect in the membrane does not occur [35].

In this paper, we present the first observations of THz-induced disassembly of polymerized and chemically stabilized microtubules. Within minutes of exposure to a train of broadband intense THz pulses, we observed intensity-dependent MT disassembly. Further, bandpass-filtered exposures suggest additional frequency-dependence. These results assist in identifying and characterizing a fundamental interaction mechanism of THz radiation with biological systems that may underlie observed phenotypic responses, which is currently considered an open question.

2. Methods

2.1. Growth of fluorescently labelled microtubules

Rhodamine-labelled fluorescent tubulin (excitation/emission at 543/590 nm) was obtained from Cytoskeleton (Denver, USA), and MTs were polymerized according to the manufacturers' instructions [37]. One aliquot of rhodamine tubulin (Cytoskeleton, TL590M) was resuspended to 5 mg/mL (45.5 µM) in 4.0 µL of general tubulin buffer (Cytoskeleton, BST01) supplemented with 0.01 volumes of 100 mM GTP (Cytoskeleton, BST06) and 1 µL of MT cushion buffer (Cytoskeleton, BST05) to facilitate polymerization. This solution was mixed with 70 µL of an equivalent solution using unlabeled tubulin (Cytoskeleton, T240) for a final labelling ratio of 1:15. Aliquots were placed in an incubator at 37°C for 20 minutes to allow the tubulin to polymerize to MTs of appropriate length (average ∼10 µm). Upon polymerization, the MTs were removed from the incubator and stabilized with 100 µL of taxol/MT buffer solution (20 µM taxol in general tubulin buffer). These were stored at room temperature as recommended, and the MTs were verified to be stable in this state for several hours. Further dilutions of this stock solution with taxol/MT buffer were performed as experimentally required. A fluorescence image of rhodamine-labelled polymerized and stabilized MTs is shown in Fig. 1(b).

2.2. Generation and detection of intense terahertz pulses

Intense THz pulses were generated by optical rectification of tilted-pulse-front laser pulses in lithium niobate ($LiNbO_3$), as schematically shown in Fig. 2(a). An oscillator/amplifier (Coherent Micra/Legend) generated a 1 kHz train of 800 nm, 50 fs, 3.6 mJ infrared laser pulses. An 1800 mm^{-1} reflective diffraction grating (RDG) established a pulse-front-tilt in the pump laser to satisfy velocity-matching conditions in the $LiNbO_3$ generation crystal with a 63° cut output face [38]. Two cylindrical focusing lenses (f_{L1}=100 mm, f_{L2}=60 mm) in a 4f configuration imaged both the laser pulse front and grating surface onto the crystal output for optimal THz emission, as described in [39].

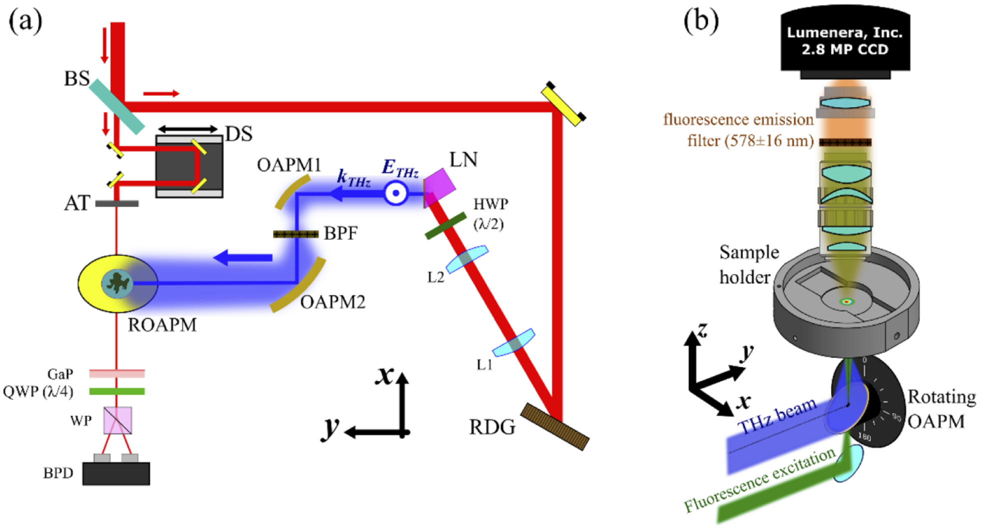

Fig. 2. THz source generation and exposure schematics. (a) The intense THz pulse source for tilted-pulse-front optical rectification in lithium niobate (LN, $LiNbO_3$), using an 1800mm^{-1} reflective diffraction grating (RDG) and a pair of 4f-imaging lenses (L1 and L2), as described in [39]. Cross-absent bandpass filters (BPF) are used to isolate individual frequency bands. The THz beam is focused to either the sample location (beam propagating in the $+z$ direction out of the page), or to the EO sampling system (beam in the $-x$ direction) with a rotating gold off-axis parabolic mirror (ROAPM). A fraction of the pump pulse energy from a beamsplitter (BS) is attenuated (AT) and propagated colinearly with the THz beam for EO sampling in gallium phosphide (GaP). (b) The ROAPM is set at 0° ($+z$, upwards) for through-substrate exposure of MTs in solution. The fluorescence excitation line is focused through the hole in the mirror and propagates to the sample colinearly with the focusing THz beam. The sample fluorescence emission is collected by long-working distance objectives, passed through a 578±16 nm bandpass filter, and analyzed in real-time with a CCD camera. For EO sampling, the ROAPM is set to 90°.

The collimated THz emission from the LN crystal was filtered with black polyethylene to remove pump leakage. The beam was magnified and re-collimated by a pair of gold off-axis parabolic mirrors (OAPM) with focal lengths of f_{OAPM1}=15 mm and f_{OAPM2}=101.6 mm for a total magnification of 6.8. The expanded, collimated beam is directed towards a 76.2 mm focal length OAPM mounted to a programmable rotation stage (Thorlabs, PRM1Z8), as shown in Fig. 2(b). This provided 360° control of the THz focus in a 76.2 mm radius annulus to focus to either the sample location (0°), or to the electro-optic (EO) sampling module for waveform detection (90°).

Temporal waveforms were detected by free-space EO sampling in a 200 µm (110) gallium phosphide (GaP) crystal mounted to a 2 mm (100) GaP substrate. Peak electric fields, E_{THz}, were calculated directly from the normalized EO signal, $\Delta I/I_0$, from balanced photodetectors (BPD) according to the equation,

$$\frac{\Delta I}{I_0} = \sin\left(\frac{2\pi L}{\lambda_0} n_0^3 r_{41} t_{GaP} E_{THz}\right) \tag{1}$$

where λ_0=800 nm is the vacuum wavelength, n_0=3.18 is the nominal GaP index, t_{GaP}=0.46 is the GaP transmission coefficient, and r_{41}=0.88 pm/V is the GaP EO coefficient [39]. Here, ΔI is the single-channel modulation of the BPD, and I_0 is the reference signal with no THz field present.

The pulse energy and transverse intensity distribution were measured with a pyroelectric detector (Spectrum Detector, SPJ-D-8) and camera (Electrophysics, PV320), respectively.

Focused spot sizes were calculated as the *1/e*^{2} width of the Gaussian fits to 1D line profiles, and pulse durations were determined as the *1/e* width of the waveform Hilbert transform. For investigations of frequency dependence, THz bandpass filters (Thorlabs, FB19M590/FB19M200, 19.6 mm inner diameter) were used as additional filtration to isolate the 0.5 THz and 1.5 THz bands. The broadband and bandpass waveforms, power spectra, and spatial intensity distributions at the focus are shown in Fig. 3. Typical pulse parameters are summarized in Table 1.

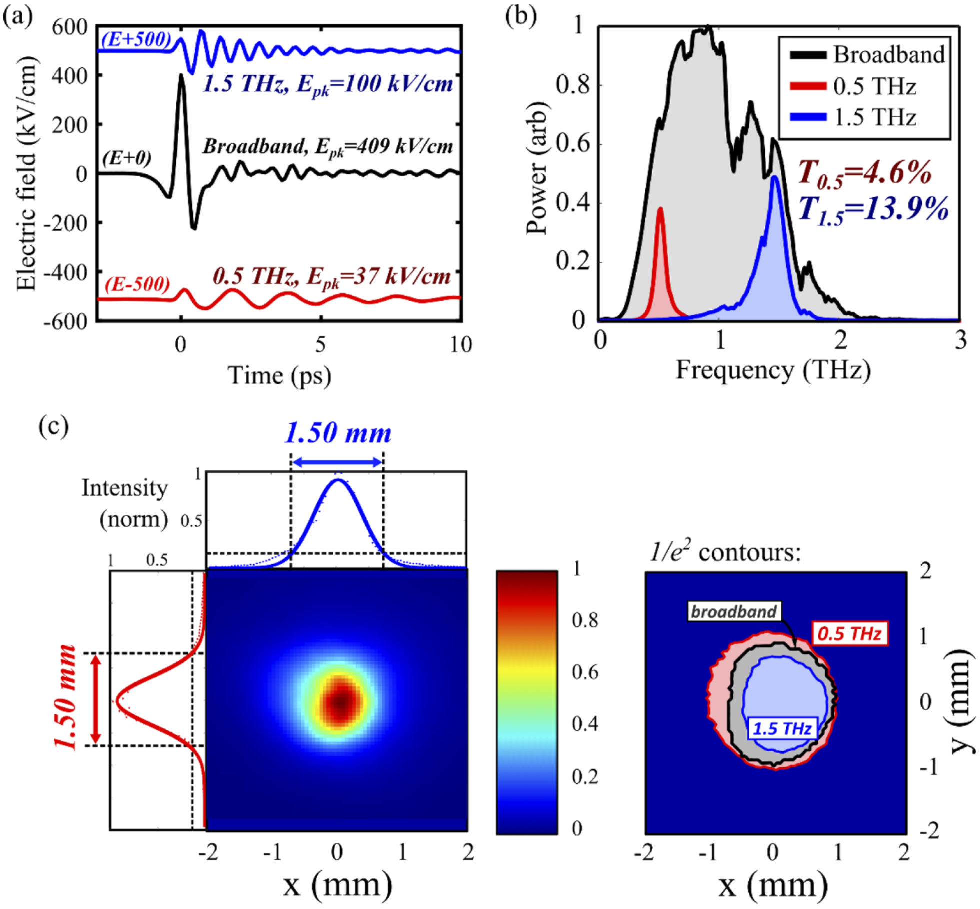

Fig. 3. Waveforms and spot areas for the intense THz pulse beam. (a) Broadband and bandpass EO sampled THz waveforms, shifted vertically for clarity. The peak broadband field and pulse energy are 409 kV/cm and 1.2 µJ, respectively. (b) The corresponding power spectra and total energy transmission factors. (c) Pyroelectric camera image of the focused THz spot. Gaussian fits to horizontal (top) and vertical (left) line profiles define the *1/e*^{2} broadband spot size as 1.5×1.5 mm^2. The contours (right) represent the *1/e*^{2} boundaries corresponding to the labelled frequency bands. Individual frequency bands that comprise the broadband pulse focus to different areas of space.

2.3. Alignment procedure for real-time analysis

To ensure the THz focus, sample location, and microscope imaging plane were coincident in space, the alignment procedure in Fig. 4 was employed. First, the THz pulse energy was maximized through a 1 mm pinhole alignment aperture placed at the sample location with a pyroelectric detector (ScienceTech, 6925-01) centered above. Once this signal was maximized,

Table 1. THz pulse parameters for MT exposures

	Broadband	0.5 THz band	1.5 THz band
Pulse Energy (μJ)	1.20 ± 0.07	0.10 ± 0.03	0.14 ± 0.02
Peak field (kV/cm)	409	37	100
Peak frequency (THz)	1.0	0.52	1.5
Bandwidth FWHM (THz)	0.6	0.07	0.2
Pulse duration[a] (ps)	1.0	6.3	2.9
Spot size[b] (mm)	1.5	2.1	1.0
Average intensity (mW/cm^2)	68 ± 4	3.0 ± 0.9	18 ± 3
Peak intensity (MW/cm^2)	68 ± 4	0.5 ± 0.1	6.2 ± 0.9

[a] Pulse durations are the *1/e*-width of the Hilbert envelope
[b] Spot sizes are the mean *1/e*^{2}-width of the Gaussian THz focus.

the detector was removed, and the microscope field-of-view (FOV) was focused to the pinhole to ensure the imaging plane and THz focus were longitudinally aligned and centered. Next, a sham sample was loaded into the holder and longitudinally translated until the sample was in focus. This achieved coincidence of the sample and image planes with the THz beam focus for the real-time fluorescence analysis of MTs.

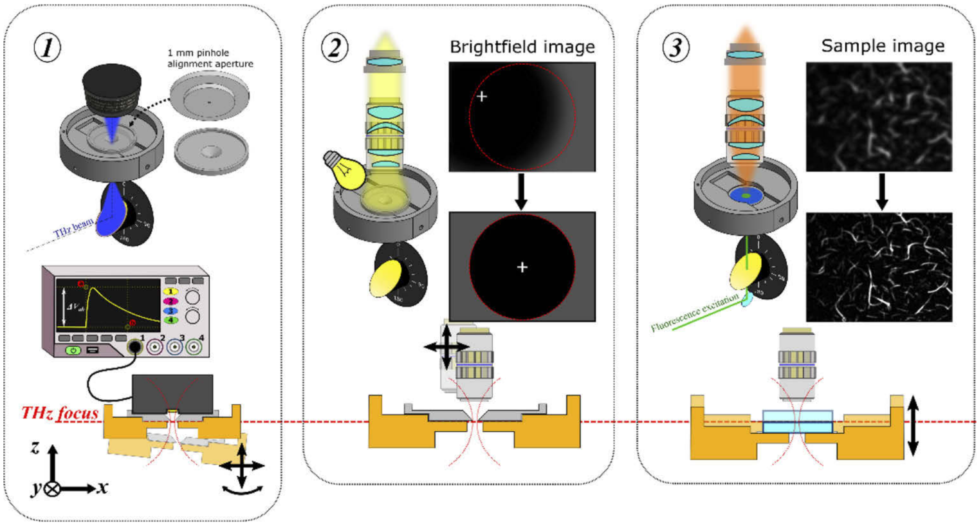

Fig. 4. Alignment procedure for light and fluorescence microscopy imaging of the THz focus and sample planes. The horizontal dashed line indicates the THz beam waist. (1) The dish is levelled, and the THz beam focus is located by translating the holder and maximizing pulse energy through a 1 mm pinhole aperture centred over the beam input window. (2) The microscope is centred (x-y) and longitudinally (z) aligned to the THz focus by bringing the alignment aperture used for THz energy measurements into focus in the brightfield FOV. (3) The sample plane for a given substrate is aligned to the THz focus by longitudinally (z) translating the sample holder until a test sample is in focus.

2.4. Microtubule exposures

MT solutions were loaded onto double-well microscope slides of optical plastic that were verified to be transmissive (T=0.92) to THz wavelengths (Ibidi μ-slide, Cat. 80281), with sufficient volume to fully cover the focused THz spot once compressed with a coverslip (1–3 µL). The MTs were left for several minutes to 1 hour to settle to the substrate and ensure stability. For exposure, the THz beam was focused through a 5 mm diameter hole in the sample holder with the rotating OAPM to one of the wells, and the second well provided matched, unexposed control solutions. Similar to the recommended MT stock storage conditions, exposures were carried out at room temperature.

2.5. Real-time fluorescence imaging and image analysis

THz-exposed rhodamine-MTs were imaged in real-time with a fluorescence microscope aligned to the beam focus. The fluorescence excitation laser (532 nm CW diode-pumped solid-state laser) was focused from below through a 1 mm hole in the rotating OAPM, and uniformly excites the sample growth area. Short pass filters eliminated any residual 805 nm and 1064 nm emissions, and a neutral density filter wheel tuned the incident power. A programmable shutter connected to the imaging camera via USB blocked the laser and allowed fluorescence excitation to be controlled within the imaging software. Fluorescence emission (~590 nm) from the sample plane was collected by long-working distance 5x/20x objectives (Mitutoyo, 378-802-6/378-804-3) and a 2x tube lens (Edmund Optics, MT-2, 56-863), passed through a 578±16 nm bandpass filter, and collected by a 2.8 MP monochrome CCD microscopy camera (Lumenera, Infinity 3-3URFM).

For each timepoint acquired during THz exposure, a series of 15 images were averaged with an exposure time of no greater than 300 ms each. The excitation laser therefore exposed the samples for no more than ~5 s for each image set. Excitation control images were acquired, and a photobleach calibration curve was experimentally determined. It was verified that the timescale for the fluorescent label to experience significant levels of photobleaching was much greater than the excitation exposure times utilized in this study. For imaging, auto-exposure control (AEC) was enabled when investigating general structural effects. In cases where the pixel intensity values were utilized for quantitative calculations (Section 3.2), AEC was disabled. Sample fluorescence images for low and high tubulin concentrations are shown in Fig. 5. Low initial tubulin concentrations result in individually resolvable MTs, while large tubulin concentrations form large aggregate structures.

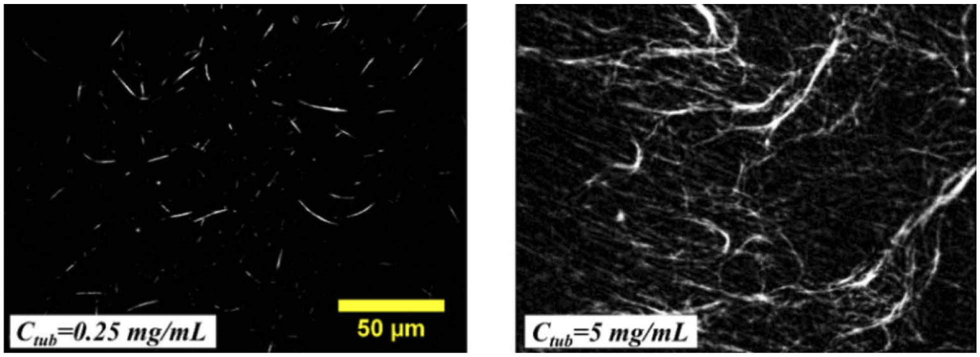

Fig. 5. Real-time fluorescence images of THz-exposed MTs. At low concentration (C_{tub}, left), MTs are individually resolvable and are stabilized at an average length of ~10 µm. At high C_{tub} (right), MTs form large aggregate structures and are not individually resolvable.

Image processing and analysis was performed using the open-source software, ImageJ (https://imagej.net). Fluorescence images were background-subtracted with a rolling-ball algorithm. For the frequency-dependent studies, the structural change to MTs were quantified by the area fraction of the image space occupied by MTs. MT area fractions were determined by first creating a binary image mask for each timepoint with a common pixel intensity threshold.

As MTs disassemble, intensity per unit area reduces, which reduces the total fraction of pixels with rhodamine fluorescence signal intensity above the chosen threshold for a given imaging region. The MT area fractions were determined with the ImageJ plugin "Analyze Particles" applied to the masked images, which algorithmically contours the masked MTs and determines the enclosed areas. Each set of MT area fractions were normalized to the initial timepoint.

3. Results

3.1. Intensity-dependence of broadband terahertz pulses on microtubule structure

Figure 6 shows three sets of time-series images from broadband THz exposures for varying exposure conditions. Differing combinations of imaging magnification (M) and tubulin concentration (C_{tub}) were utilized to analyze either single or aggregate MT structures in either uniform or non-uniform intensity distributions.

High-M and low-C_{tub} experiments (40x, 0.25 mg/mL) provide detailed structural resolution to individual MTs. As shown in Fig. 6(a), disassembly of a single MT is shown to occur within 11 minutes with 0.8 μJ pulses and a 230 kV/cm peak field strength. A multimedia file of the single MT breaking in Fig. 6(a) is included (see Visualization 1).

Low-M and High-C_{tub} (10x, 5 mg/mL) experiments with similar exposure parameters show the large-scale effects to MT aggregates (Fig. 6(b)). The large FOV allows analysis of intensity-dependence within a single exposure: By analyzing structural effects to MTs for varying distances from the center of the THz focus, differential effects to MT structure for varying energy densities are investigated. From within the total imaging FOV of 870×655 μm^2, three 100×100 μm^2 FOVs were selected for analysis, corresponding to different regions of the THz intensity distribution (shown at right in Fig. 6(b)). In the central region, the energy density reaches 80 $\mu J/cm^2$, and the largest qualitative change to MT structure is observed. Near the beam edge ~0.5 mm from center, the energy density falls to ~30 $\mu J/cm^2$, and no significant structural change is observed.

High-M and High-C_{tub} (40x, 5 mg/mL) experiments show structural effects to MT aggregates in a nearly uniform THz intensity profile at higher THz pulse energy (1.2 μJ) and field strength (400 kV/cm and 409 kV/cm), depicted in Fig. 6(c). In both time-series, MT disassembly and aggregate destruction occurs significantly faster than the previous exposure cases, within ~5 minutes, further corroborating the evidence for intensity-dependence that was indicated in the differential effects seen in the low-magnification images.

3.2. Exposures with terahertz bandpass filters

From the broadband exposure results in Section 3.1, it is not possible to conclude that the observed effects are strictly only intensity-dependent, since wavelength-dependent focusing induces spatial variation in frequency for the broadband pulse, in addition to the power-density variation. The central intense region of the beam contains a larger fraction of high frequency energy relative to the low-intensity beam regions, and so the differential effect to large MT aggregates for varying location in the THz focus may additionally be influenced by the frequency distribution associated with the region of space under consideration.

To isolate the potential effects for varying spectral content, THz bandpass filters are used to transmit narrow 0.5 THz and 1.5 THz bands, and compared to broadband exposure, adjusted for intensity differences. For these analyses, THz-induced MT disassembly is quantified using the MT area fraction. As shown in Fig. 7(a), contours determined with the analysis algorithm (Section 2.5) define this area fraction, which decreases over time as the fluorescence signal from disassembled MTs falls below the mask threshold. The results in Fig. 7(b) show that the decrease in MT area generally follows an exponential decay. For comparison, an equivalent analysis with images of unexposed MTs is included. The curves are labelled with characteristic times from fitting these data to an exponential function to establish quantitative timescales of THz-induced

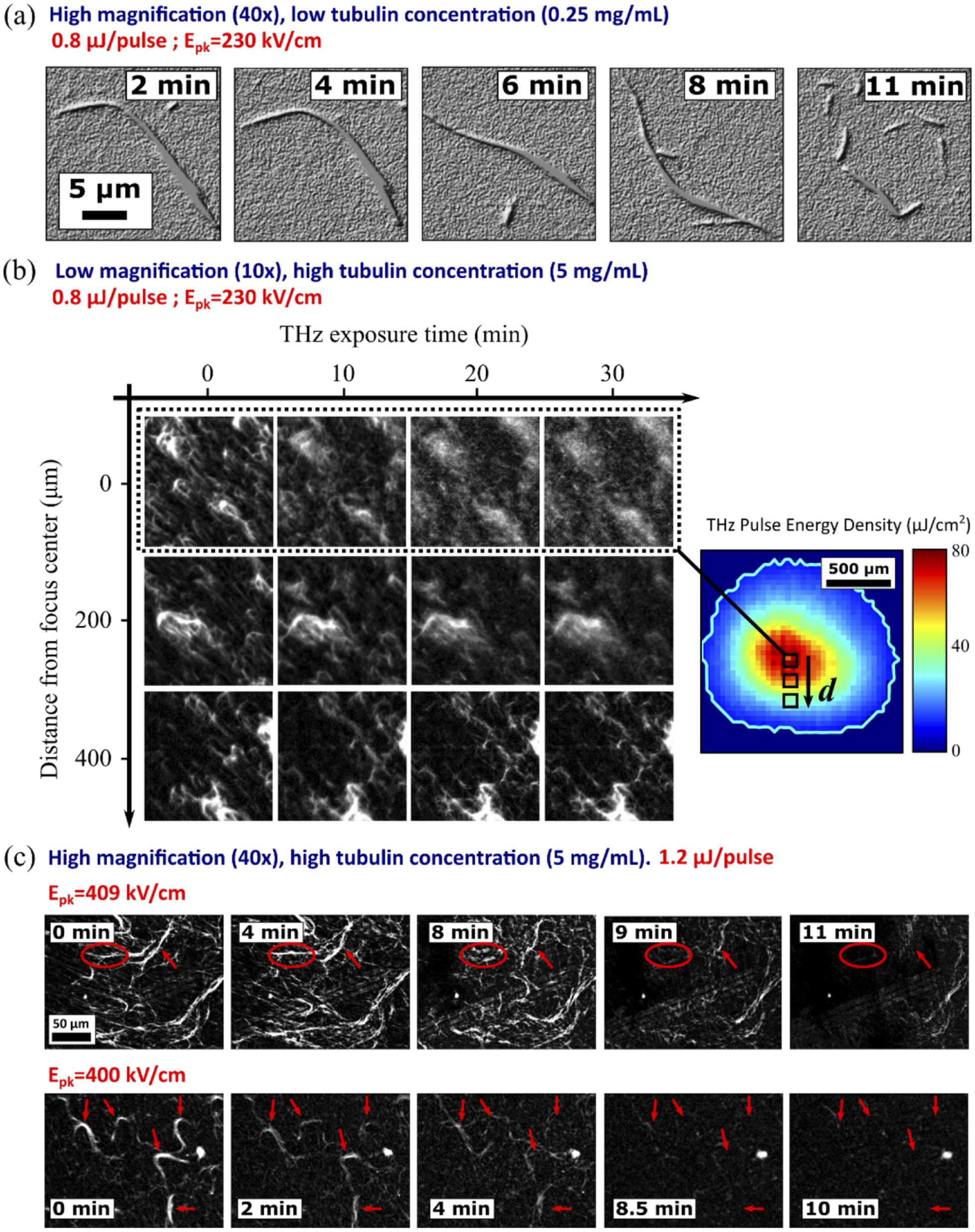
(a) High magnification (40x), low tubulin concentration (0.25 mg/mL)
0.8 μJ/pulse ; E_pk=230 kV/cm
2 min
4 min
6 min
8 min
11 min
5 μm
(b) Low magnification (10x), high tubulin concentration (5 mg/mL)
0.8 μJ/pulse ; E_pk=230 kV/cm
THz exposure time (min)
0
10
20
30
Distance from focus center (μm)
0
200
400
THz Pulse Energy Density (μJ/cm²)
500 μm
d
80
40
0
(c) High magnification (40x), high tubulin concentration (5 mg/mL). 1.2 μJ/pulse
E_pk=409 kV/cm
0 min
4 min
8 min
9 min
11 min
50 μm
E_pk=400 kV/cm
0 min
2 min
4 min
8.5 min
10 min

Fig. 6. Broadband MT exposure results. (a) High magnification (40x) fluorescence images of low tubulin concentration (0.25 mg/mL) show detailed structural disassembly to individual MTs. A single motion-tracked MT disassembling within 11 minutes of THz exposure. The ImageJ hill-shade algorithm is utilized to enhance edge contrast. (b) Low magnification (10x) images of high tubulin concentration (5 mg/mL) show large-scale disassembly of MT aggregate structures in a varying intensity distribution. The three sets of time-series images correspond to three 100×100 μm^2 regions indicated in the THz spot image (right), having approximate energy densities of 80, 50, and 30 $\mu J/cm^2$. Greater disassembly is observed in the highest intensity central region. (c) High magnification (40x) and high tubulin concentration (5 mg/mL) show MT aggregates in a nearly uniform intensity FOV. Both time series are separate results with similar pulse energy (1.2 μJ) and peak field (409 kV/cm [top] and 400 kV/cm [bottom]). At larger THz energy and field strengths, significant MT disassembly is observed within 5 min. Red labels highlight regions of MT polymer breakage.

effect for varying spectral content. The top plot of Fig. 7(b) shows the total pixel intensity of the images for each timepoint. The maximum loss of total fluorescence signal was ~5%, and so the decrease in MT area fraction of THz-exposed samples is not due to photobleaching of the rhodamine label, but rather to MT disassembly, as illustrated in the second column of Fig. 7(a).

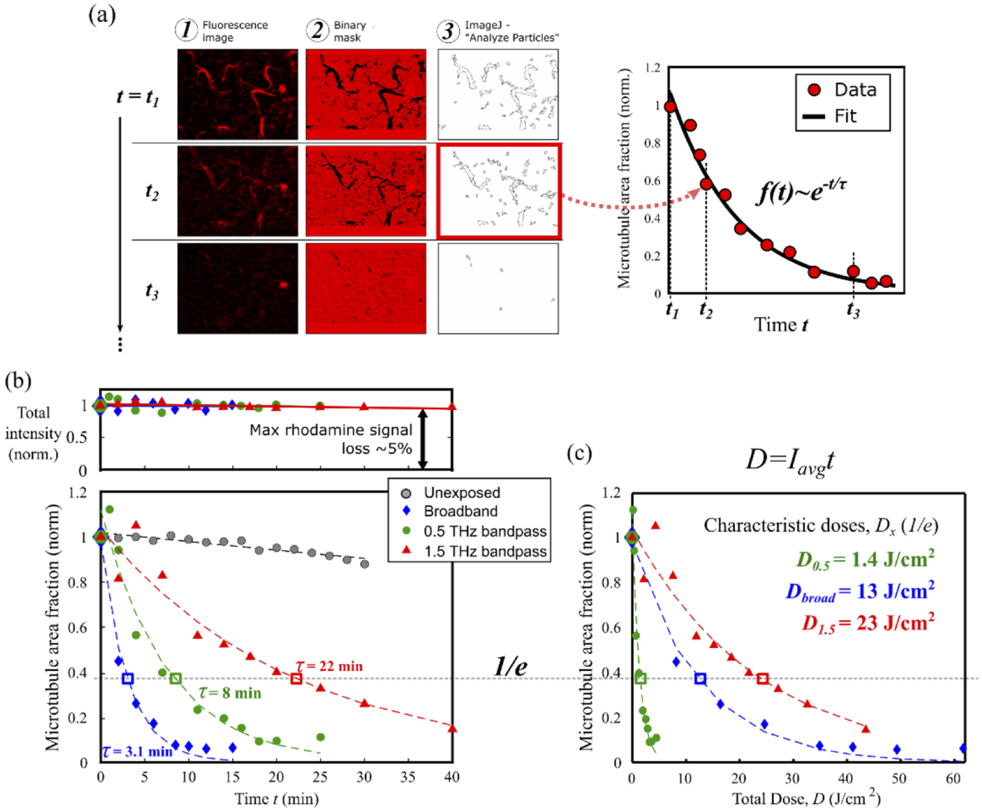

Fig. 7. Analysis and results of MT exposures with varying spectral content. (a) An example image analysis of MT structural change. By converting quantitative fluorescence images (column 1) to a binary image with a common threshold (column 2), the disassembly of MTs over time may be quantified by the change of area fraction with rhodamine signal above a common intensity threshold. The area fractions are determined by algorithmic contours with the ImageJ plugin, "Analyze Particles". The reduction of area fractions follow an exponential decay curve. (b) Fractional MT area calculated using the procedure in (a) for varying THz bands, with dashed curves representing exponential fits, and τ is the associated characteristic time. Each dataset was normalized to the initial relative MT area. The exponential fit qualities (R^2) are 0.99, 0.96, and 0.92 for the broadband, 0.5 THz, and 1.5 THz fits, respectively. An equivalent analysis on unexposed MTs is included for reference. *Top:* The total pixel intensity of the raw images. The total rhodamine signal of all images does not degrade significantly (<5%) over the exposure duration, indicating the MT area fraction decay is not due to photobleaching. (c) The MT area fraction vs. total dose (J/cm^2), which corrects for differences in pulse energy and focused spot area (see Table 1). D_X is the characteristic dose for the corresponding curve (e^{-D/D_X}) . The characteristic total dose for the low-frequency 0.5 THz band (1.4 J/cm^2) is significantly lower than both the broadband and high-frequency 1.5 THz band (13 J/cm^2 and 23 J/cm^2, respectively), indicating frequency-dependence of THz-induced MT disassembly, with greater disassembly induced by low-frequency THz energy (~0.5 THz).

While there is a large range of characteristic times for varying spectral content from the fits in Fig. 7(b), this could be due to differences in pulse energy and focused spot area between the separate THz pulses (Fig. 3, Table 1). To correct for these differences, the MT area fraction is plotted as a function of the total dose, $D = I_{avg}t$, as shown in Fig. 7(c). The total dose is reported in units of J/cm^2, and is distinct from the per-pulse energy density (µJ/cm^2) in Fig. 6. The difference in characteristic doses indicate that THz-induced disassembly of MTs is significantly influenced by the pulse frequency content, as discussed in the following section.

4. Discussion

Exposures at higher magnification (40x) and low tubulin concentration (0.25 mg/mL) provide an opportunity to observe detailed effects resolvable to single MTs (Fig. 6(a)). Conversely, analysis of low-magnification (10x), high-concentration (5 mg/mL) MT samples are used to investigate intensity-dependence in a single exposure by analyzing separate regions of the imaging FOV for varying locations in the Gaussian intensity distribution (Fig. 6(b)). In the former case, disassembly of a single MT polymer is observed to occur within 11 minutes of THz exposure. In the latter case, significant variation in THz-induced change to MT structure is observed for varying locations within the THz focus over the exposure duration. The strongest effect is observed in the central region with the highest intensity (top row of Fig. 6(b)), in which the blurring of large aggregate structures is attributed to single MTs disassembling, as in Fig. 6(a). As the analysis window moves to the lower-intensity outer area of the beam, the magnitude of the effect diminishes.

The above cases were exposed with a moderately attenuated THz beam (0.8 µJ/pulse, 230 kV/cm), and the disassembly to MTs occurred in 11 minutes. Figure 6(c) shows high-concentration exposures with higher pulse energy (1.2 µJ/pulse) and field strength (400 kV/cm and 409 kV/cm), and at high magnification such that the THz intensity profile is roughly uniform across the imaging FOV. Here, initiation of MT structure changes is observed within 4–6 minutes, further supporting the intensity-dependence observed above.

4.1. Frequency-dependence

Exposures at high magnification (40x) and high tubulin concentration (5 mg/mL) with THz bandpass filters investigated coarse frequency-dependence within an approximately uniform intensity distribution across the imaging FOV. The characteristic times for MT disassembly extracted from the exponential fits in Fig. 7(b) are 8±2 min (R^2=0.9626) and 22±6 min (R^2=0.9223) for the 0.5 THz and 1.5 THz bands, respectively. While these are significantly longer than the broadband reference case (τ=3.1±0.6 minutes, R^2=0.9854), they also correspond to significantly lower pulse energy, intensity, and peak electric field, as summarized in Table 1.

Figure 7(c) shows the MT area fraction curves in terms of dose delivered (J/cm^2), which corrects for differences in pulse energy and area, but not peak electric field. If effects depended only on intensity, the corrected curves are expected to overlap. However, the characteristic dose for the 0.5 THz band is 1.4±0.3 J/cm^2, relative to 23±6 J/cm^2 for the 1.5 THz band. Additionally, the field strength of the 0.5 THz band (37 kV/cm) is significantly lower than the 1.5 THz field strength (100 kV/cm). Since the 0.5 THz disassembly occurs faster not only at a lower dose, but also a lower peak field strength, these data indicate that MT disassembly is significantly influenced by frequency content. The broadband curve corresponds to a characteristic dose of 13±3 J/cm^2, intermediate to the curves for the low and high frequency bands. This suggests that the observed broadband MT disassembly is predominantly due to low-frequency energy, while much of the high-frequency content is not utilized for MT disassembly, but is likely instead absorbed by the media or thermalized.

Other effects may potentially explain the observed frequency dependence as well, such as differential absorption in the aqueous media environment prior to MT interaction. In water, the absorption coefficients at 0.5 THz and 1.5 THz are approximately 82.6 cm^{-1} and 153.6 cm^{-1}, respectively, and so more of the high-frequency band will be absorbed in aqueous media rather than the MTs [40]. Additionally, in MTs the calculated absorbed energy at 1.5 THz is also roughly twice the energy absorbed at 0.5 THz, and so these competing effects obscure one another experimentally [5]. Future studies investigating concentration dependence (i.e., varying probabilities of THz absorption in MT structures relative to surrounding media) or variation of aqueous media layer thickness (i.e., varying interaction distance in the MT solution) will assist in contextualizing these apparent frequency-dependent effects to better understand the precise nature of this interaction.

4.2. *Considerations of thermal or shockwave interaction mechanisms*

An important consideration is the potential for other interaction mechanisms, such as thermal effects or field-induced shockwaves, to influence the biological response in THz exposure studies [15,27]. In our experiments, the duty cycle is limited (1 kHz train of picosecond-duration pulses) to ensure negligible heating in the biological media. An estimate of the maximum per-pulse temperature increase from the broadband THz pulse is roughly 5 mK, using $\Delta Q = mc\Delta T = \rho Vc\Delta T$, where ΔT is the temperature change due to a pulse energy ΔQ, and assuming similar properties to water (density ρ=1 g/cm^3, specific heat capacity c=4.2 J/g/K). The volume $V = Az$ is calculated from the THz spot area and penetration depth. The average steady-state heating due to the 1 kHz pulse train is measured with a thermal imager (Reed Instruments, R2100) to be less than 1°C in water, and is consistent with measurements of other similar THz exposure systems [41–43]. These are also consistent with the THz-water heating model from Kristensen et al., which predicts a maximum temperature change at the beam center of 2°C for our broadband beam parameters [44].

In addition to the measurements above, experiments with taxol-stabilized MTs inherently control for thermal effects, as they are verified to be stable for several hours at room temperature, and higher temperatures assist MT polymerization (indeed, it is the mechanism exploited to polymerize MTs from tubulin by placing them into a 37°C incubator, as described in Section 2.1). Therefore, disassembly by THz represents the opposite effect to that expected from increasing sample temperature. This implies that the dominant interaction mechanism is non-thermal and may instead be explained by coupling to natural oscillatory dynamics of MT structures.

Using intense THz pulses generated by a free electron laser, Yamazaki et al. induced dramatic disassembly of actin polymers within 30 minutes that was attributed to an acoustic shockwave formed in the aqueous medium that penetrates significantly deeper than EM THz energy [27]. While this represents an exciting new interaction mechanism to explore that may play a role in THz-induced biological effects, we cannot claim with confidence that similar shockwave phenomena are occurring in the present study. Tsubouchi et al. show that the acoustic shockwave amplitude is expected to scale linearly with the product of absorption coefficient and fluence, αF, with significant shockwave amplitude requiring αF on the order of ~0.1–1 J/cm^3 [45]. The relatively lower values in our work ($\alpha F < 0.02$ J/cm^3) may not be sufficient to produce acoustic waves with significant amplitude, although this should be explored as a potential mechanism in future investigations. Nevertheless, we observed MT disassembly within minutes at similar fluence, but with lower acoustic generation efficiency.

4.3. *Relation to tissue-level biological effects*

Recently, we have reported on differential gene expression induced by intense THz pulses in human skin, and identified biological processes predicted to be dysregulated [46]. In these experiments, 3D human skin tissue models were exposed using similar beam parameters (2.4 µJ/pulse, $E_{peak} = 240$ kV/cm, $I_{pulse} = 74$ MW/cm^2) as those outlined in Section 2.2. Here, we emphasize additional aspects of these data in the context of the MT exposures presented in this paper. Specifically, these are the THz-induced gene expression of tubulin and microtubule-associated genes in human skin, and the predicted dysregulation of cytoskeleton-related processes at the tissue-level of biological organization.

Figure 8(a) shows the differential gene expression induced by intense THz pulses of all genes in the tubulin superfamily and genes that encode for microtubule-associated proteins (MAPs). Intense THz pulses largely downregulate expression of tubulin and other genes related to MT structure and function. There is a particularly large suppression of genes in the α and β subfamilies (TUBA and TUBB), which encode for the principal structural components of MTs, as described in Section 1. Gamma and delta tubulin, which play critical roles in MT nucleation, were unaffected. In the context of the significant disassembly of MTs induced by THz pulses presented in this study, this differential gene expression may represent the cell's genomic response to a disassembled and disrupted cytoskeletal network.

Downregulation of TUBA and TUBB following chemical disassembly of MTs in human cells has been established for decades [47–50], further corroborating the significance of THz-induced MT disassembly as a key mechanism driving the tissue-level biological response in skin in Fig. 8(a). However, more work needs to be done to elucidate the precise nature of this potential THz interaction mechanism. Among the other microtubule-regulating genes affected by THz are the microtubule-associated protein (MAP) family that regulate MT growth, and PLK4, a serine/threonine kinase that regulates mitotic centriole dynamics [51]. With the exception of TTL, a cytosolic enzyme responsible for post-translational modifications of alpha tubulin, all significant THz-induced effects on MT-associated gene expression were inhibitory.

Some of these THz-affected genes have also been investigated for therapeutic application in gene therapy: Knockdown of class II, III, or IV β-tubulin family genes (TUBB2A, TUBB2C, TUBB4Q, and TUBB3 in Fig. 8(a)) has been shown to enhance the effectiveness of tubulin-binding pharmacological agents via suppression of MT dynamics and sensitization to apoptosis induction [52,53]. These data motivate the hypothesis that intense THz pulses may enhance the sensitivity of diseased cells to similar drugs via interaction with MTs and potentially other cytoskeletal structures.

Gene Ontology (GO) analysis was performed on the measured expression dataset to identify statistical over-representations of biological processes, cellular components, and molecular functions among the set of significantly differentially expressed genes, relative to expected global background rates [54]. 58 total GO terms were identified as over-represented by the THz-induced expression profile ($p<0.01$). These were largely related to epidermal processes (as the sample under study was skin), however, 8 GO terms were associated with general or specific cytoskeletal processes, components, and functions. The GO terms, odds-ratios (OR), and p-values are shown in Fig. 8(b), and include over-representation of THz-affected genes in several important cytoskeleton-regulated processes. Thus, intense THz pulses may dysregulate these cytoskeletal-related functions leading to phenotypic changes observed at cellular or tissue levels. In the future, studies explicitly investigating THz-induced changes to MTs or other cytoskeleton protein complexes correlated to the expression dynamics of genes identified in Fig. 8(a) will assist in clarifying the precise nature of the cellular response to THz-MT interactions.

The present study shows that intense THz pulses are capable of dissociating cellular concentrations of polymerized, taxol-stabilized MTs within minutes of application, and are consistent with differential gene regulations measured in cellular systems. The onset of MT disassembly is dramatic and clearly triggered by THz power input, as seen in repeated, controlled experiments. Nonetheless, several exposures have also been performed in which no effect to MT structure was observed, even in similar exposure conditions that had previously induced disassembly. Since MTs are verified to be stable at room temperature for hours, spontaneous disassembly in controlled exposure studies is likely not occurring. The most likely explanation is that our current THz sources, while sufficient to induce MT disassembly under optimal conditions, are

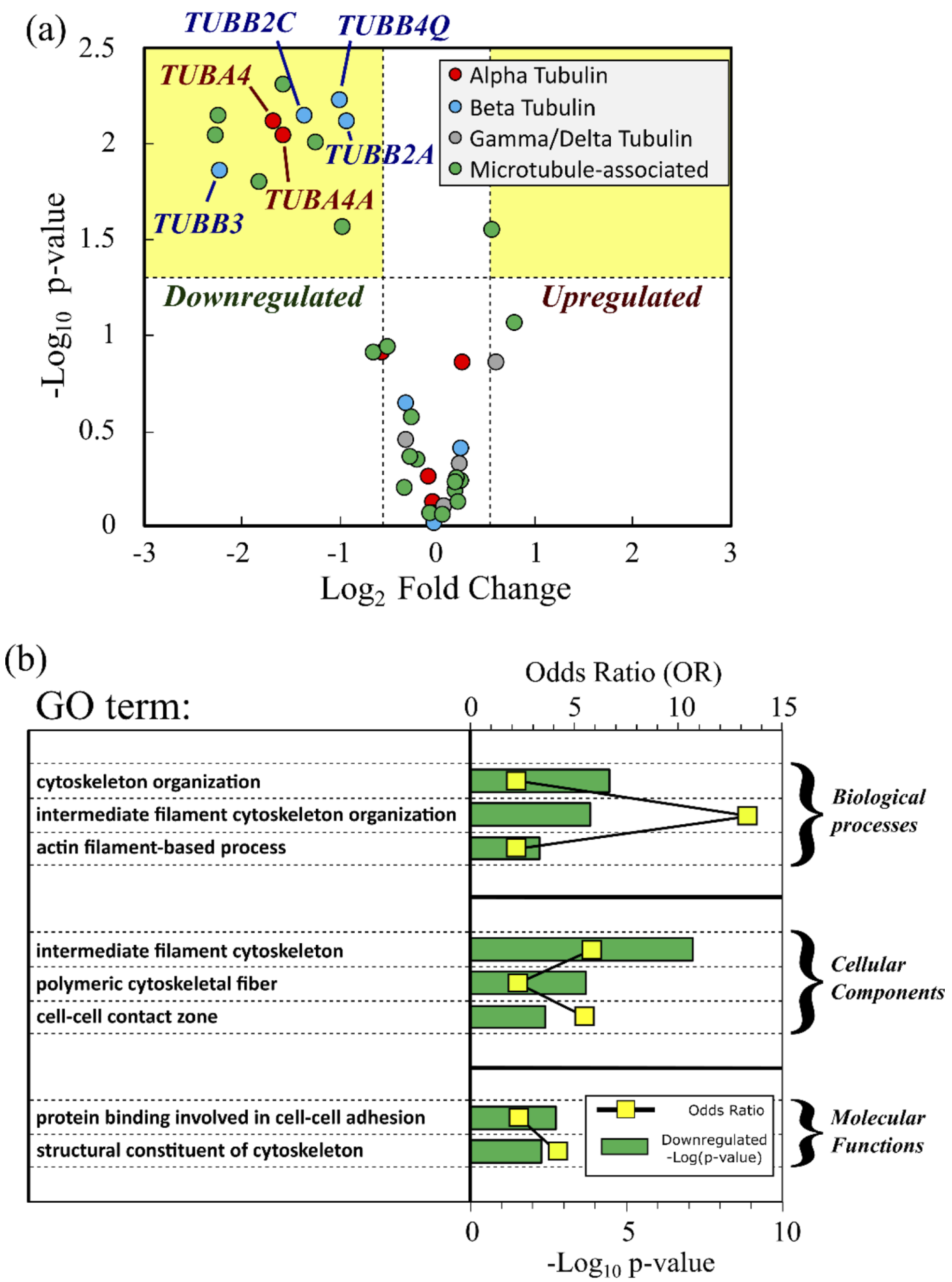

Fig. 8. Intense THz pulses significantly downregulate several members of tubulin/MT gene families. (a) Volcano plot showing differential expression of the tubulin superfamily and other microtubule-associated genes induced by intense THz pulses in human skin. Dashed lines indicate conventional thresholds of expression significance ($|\mathrm{Log}_2(I/I_0)| > 0.58$, $p < 0.05$). Genes that encode for structural α/β tubulin (TUBA/TUBB) subunits are significantly downregulated. (b) Gene Ontology (GO) analysis of the global expression dataset identifies significant over-representation in eight cytoskeleton-related processes, components, and functions.

close to the levels necessary for detectable MT disassembly, as suggested by the diminished effect near the outer regions of the beam, but still within the defined THz focus (Fig. 6(b)). Small variations in the MT environment may significantly affect the THz energy and field such that the pulse seen by the sample is rendered insufficient for significant MT disassembly. These data suggest that THz-induced disassembly requires energy density in the range of 30–80 $\mu J/cm^2$, a peak-field strength $>$ 37 kV/cm, total dose on the order of $\sim$1–10 J/cm^2, and a further dependence on spectral content of the THz pulse, with faster disassembly for low-frequency THz bands ($\sim$0.5 THz). More research investigating the THz parameter space for differential structural change is necessary.

The inhibition of MT dynamics is a standard mechanism of action for several types of pharmacological agents used in chemotherapy. Paclitaxel (also known as taxol, the MT stabilizing agent used in these experiments) is an early chemotherapy drug that inhibits MT dynamics by stabilizing polymerized filaments such that necessary cycles of polymerization/depolymerization (“treadmilling”) are suppressed [3,55]. Similarly, colchicine is an experimental anti-cancer (and anti-inflammatory) drug that inhibits tubulin dimers from polymerizing into MT filaments [56]. Several other types of tubulin-binding pharmacological agents such as vinblastine, demecolcine, or nocodazole, similarly inhibit MT dynamics and reduce polymer mass [57].

5. Conclusions

In this paper, microtubule disassembly by intense THz pulses was investigated. Significant disassembly of MTs is observed within several minutes of THz power input, and these effects are not explained by heating or shockwave formation. Significant intensity dependence was observed in the rate of MT disassembly. Moreover, exposures using THz bandpass filters suggest that the frequency content has a significant influence on the detected structural changes. However, more work is required to isolate confounding variables in exposure experiments, such as the reduction in THz energy transmitted through aqueous media, relative to the increased absorption in MTs at higher frequencies. Our results were analyzed in the context of our previous THz exposures performed in skin tissue, and suggest that MT disassembly by intense THz pulses may be a key interaction mechanism driving the biological response observed in higher-level systems like multicellular tissue.

As MTs are essential mitotic structures and popular targets of anti-cancer therapies, the THz-induced effects to MT structure reported in this paper suggest a potential therapeutic mechanism of intense THz pulses, possibly in combination with existing pharmacological interventions. Future research investigating these effects in higher-level cellular and tissue systems is necessary to establish the prospective clinical feasibility.

Funding. Alberta Innovates - Technology Futures; Canadian Foundation for Innovation; Natural Sciences and Engineering Research Council of Canada.

Acknowledgments. We thank Beipei Shi, Greg Popowich, and James Chaulk for technical assistance, and Matt Reid for use of the pyroelectric camera.

Disclosures. The authors declare no conflicts of interest.

Data availability. Data underlying the results presented in this paper are not publicly available at this time but may be obtained from the authors upon reasonable request.

References

1. D. A. Fletcher and R. D. Mullins, “Cell mechanics and the cytoskeleton,” Nature **463**(7280), 485–492 (2010).
2. R. Philips, J. Kondev, J. Theriot, and H. Garcia, *Physical Biology of the Cell* (Garland Science, 2013).
3. R. L. Margolis and L. Wilson, “Microtubule treadmilling: what goes around comes around,” BioEssays **20**(10), 830–836 (1998).
4. A. Ayoub, T. Craddock, M. Klobukowski, and J. Tuszynski, “Analysis of the strength of interfacial hydrogen bonds between tubulin dimers using quantum theory of atoms in molecules,” Biophys. J. **107**(3), 740–750 (2014).
5. J. M. Moix, J. E. Parker, and I. Echchgadda, “Qualitative behavior of the low-frequency vibrational dynamics of microtubules and the surrounding water,” J. Phys. Chem. B **121**(14), 3024–3031 (2017).

6. O. Smolyanskaya, N. Chernomyrdin, A. Konovko, K. Zaytsev, I. Ozheredov, O. Cherkasova, M. Nazarov, J.-P. Guillet, S. Kozlov, Y. V. Kistenev, J.-L. Coutaz, P. Mounaix, V. Vaks, J.-H. Son, H. Cheon, and V. Wallace, "Terahertz biophotonics as a tool for studies of dielectric and spectral properties of biological tissues and liquids," Prog. Quantum Electron. **62**, 1–77 (2018).
7. J.-H. Son, *Terahertz Biomedical Science and Technology* (CRC, 2014).
8. H. M. Berman, J. Westbrook, Z. Feng, G. Gilliland, T. N. Bhat, H. Weissig, I. N. Shindyalov, and P. E. Bourne, "The Protein Data Bank," Nucleic Acids Res. **28**(1), 235–242 (2000).
9. E. Pickwell and V. P. Wallace, "Biomedical applications of terahertz technology," J. Phys. D: Appl. Phys. **39**(17), R301–R310 (2006).
10. L. H. Eadie, C. Reid, A. Fitzgerald, and V. Wallace, "Optimizing multi-dimensional terahertz imaging analysis for colon cancer diagnosis," Expert Systems with Applications **40**(6), 2043–2050 (2013).
11. A. Panwar, A. Singh, A. Kumar, and H. Kim, "Terahertz imaging system for biomedical applications: current status," Int. J. Eng. Technol. **13**(2), 33–39 (2013).
12. T. Bowman, T. Chavez, K. Khan, J. Wu, A. Chakraborty, N. Rajaram, K. Bailey, and M. El-Shenawee, "Pulsed terahertz imaging of breast cancer in freshly excised murine tumors," J. Biomed. Opt. **23**(02), 1–13 (2018).
13. A. I. Nikitkina, P. Y. Bikmulina, E. R. Gafarova, N. V. Kosheleva, Y. M. Efremov, E. A. Bezrukov, D. V. Butnaru, I. N. Dolganova, N. V. Chernomyrdin, O. P. Cherkasova, A. A. Gavdush, and P. S. Timashev, "Terahertz radiation and the skin: a review," J. Biomed. Opt. **26**(04), 1–26 (2021).
14. M. H. Arbab, D. P. Winebrenner, T. C. Dickey, A. Chen, M. B. Klein, and P. D. Mourad, "Terahertz spectroscopy for the assessment of burn injuries in vivo," J. Biomed. Opt. **18**(7), 077004 (2013).
15. G. Wilmink and J. Grundt, "Invited review article: current state of research on biological effects of terahertz radiation," J. Infrared, Millimeter, Terahertz Waves **32**(10), 1074–1122 (2011).
16. M. Mattsson, O. Zeni, and M. Simko, "Is there a biological basis for therapeutic applications of millmeter waves and THz waves?" J. Infrared, Millimeter, Terahertz Waves **39**(9), 863–878 (2018).
17. T. Kleine-Ostmann, C. Jastrow, K. Baaske, B. Heinen, M. Schwerdtfeger, U. Karst, H. Hintzsche, H. Stopper, M. Koch, and T. Schrader, "Field Exposure and Dosimetry in the THz Frequency Range," IEEE Trans. Terahertz Sci. Technol. **4**(1), 12–25 (2014).
18. O. P. Cherkasova, D. S. Serdyukov, A. S. Ratushnyak, E. F. Nemova, E. N. Kozlov, Y. V. Shidlovskii, K. I. Zaytsev, and V. V. Tuchin, "Effects of Terahertz Radiation on Living Cells: a Review," Opt. Spectrosc. **128**(6), 855–866 (2020).
19. B. S. Alexandrov, V. Gelev, A. R. Bishop, A. Usheva, and KØ Rasmussen, "DNA breathing dynamics in the presence of a terahertz field," Phys. Lett. A **374**(10), 1214–1217 (2010).
20. L. Titova, A. Ayesheshim, A. Golubov, D. Fogen, R. Rodriguez-Juarez, F. Hegmann, and O. Kovalchuk, "Intense THz pulses cause H2AX phosphorylation and activate DNA damage response in human skin tissue," Biomed. Opt. Express **4**(4), 559–568 (2013).
21. L. Titova, A. Ayesheshim, A. Golubov, R. Rodriguez-Juarez, R. Woycicki, F. Hegmann, and O. Kovalchuk, "Intense THz pulses down-regulate genes associated with skin cancer and psoriasis: a new therapeutic avenue?" Sci. Rep. **3**, 2363 (2013).
22. H. Cheon, H.-J. Yang, S.-H. Lee, Y. A. Kim, and J.-H. Son, "Terahertz molecular resonance of cancer DNA," Sci. Rep. **6**(1), 37103 (2016).
23. J. Tang, J. Ma, L. Guo, K. Wang, Y. Yang, W. Bo, L. Yang, Z. Wang, H. Jiang, Z. Wu, B. Zeng, and Y. Gong, "Interpretation of the molecular mechanism of the electroporation induced by symmetrical bipolar picosecond pulse trains," BBA - Biomembranes **1862**(5), 183213 (2020).
24. A. Ramundo-Orlando, G. P. Gallerano, P. Stano, A. Doria, E. Giovenale, G. Messina, M. Cappelli, M. D'Arienzo, and I. Spassovsky, "Permeability Changes Induced by 130 GHz Pulsed Radiation on Cationic Liposomes Loaded With Carbonic Anydrase," Bioelectromagnetics **28**(8), 587–598 (2007).
25. "Tera-Hertz radiation in biological research, investigations on diagnostics and study on potential genotoxic effects (THz-BRIDGE), Final Report," [Online]. Available: https://www.frascati.enea.it/THz-BRIDGE/.
26. S. Yamazaki, M. Harata, T. Idehara, K. Konagaya, G. Yokoyama, H. Hoshina, and Y. Ogawa, "Actin polymerization is activated by terahertz irradiation," Sci. Rep. **8**(1), 9990 (2018).
27. S. Yamazaki, M. Harata, Y. Ueno, M. Tsubouchi, K. Konagaya, Y. Ogawa, G. Isoyama, C. Otani, and H. Hoshina, "Propagation of THz irradiation energy through aqueous layers: Demolition of actin filaments in living cells," Sci. Rep. **10**(1), 9008 (2020).
28. H. Hintzsche, C. Jastrow, T. Kleine-Ostmann, H. Stopper, E. Schmid, and T. Schrader, "Terahertz radiation induces spindle disturbances in human-hamster hybrid cells," Radiat. Res. **175**(5), 569–574 (2011).
29. A. Amicis, S. D. Sanctis, S. D. Cristofaro, V. Franchini, F. Lista, E. Regalbuto, E. Giovenale, G. P. Gallerano, P. Nenzi, R. Bei, M. Fantini, M. Benvenuto, L. Masuelli, E. Coluzzi, C. Cicia, and A. Sgura, "Biological effects of in vitro THz radiation exposure in human foetal fibroblasts," Mutat. Res., Genet. Toxicol. Environ. Mutagen. **793**, 150–160 (2015).
30. X. G. Peralta, J. C. Cantu, C. Z. Cerna, and I. Echchgadda, "Impact of sub-millimeter waves on the assembly kinetics of microtubules," *2018 43rd International Conference on Infrared, Millimeter, and Terahertz Waves (IRMMW-THz)*, 2018, 1 (2018).

31. S. Romanenko, D. Appadoo, N. Lawler, S. I. Hodgetts, A. R. Harvey, and V. P. Wallace, "Terahertz radiation stimulates neurite growth in PC12 derived neurons during development phase: preliminary study," *2020 45th International Conference on Infrared, Millimeter, and Terahertz Waves (IRMMW-THz)*, 2020, 1(2020).
32. J. J. Timmons, J. Preto, J. A. Tuszynski, and E. T. Wong, "Tubulin's response to external electric fields by molecular dynamics simulations," PLoS One **13**(9), e0202141 (2018).
33. P. Marracino, D. Havelka, J. Prusa, M. Liberti, J. Tuszynski, A. T. Ayoub, F. Apollonio, and M. Cifra, "Tubulin response to intense nanosecond-scale electric field in molecular dynamics simulation," Sci. Rep. **9**(1), 10477 (2019).
34. J. Prusa, A. T. Ayoub, D. E. Chafai, D. Havelka, and M. Cifra, "Electro-opening of a microtubule lattice in silico," Computational and Structural Biotechnology Journal **19**, 1488–1496 (2021).
35. L. Rems and D. Miklavcic, "Tutorial: Electroporation of cells in complex materials and tissue," J. Appl. Phys. **119**(20), 201101 (2016).
36. P. Vernier, Z. Levine, M.-C. Ho, S. Xiao, I. Semenov, and A. Pakhomov, "Picosecond and terahertz perturbation of interfacial water and electropermeabilization of biological membranes," J. Membr. Biol. **248**(5), 837–847 (2015).
37. Cytoskeleton Inc. - The Protein Experts, "Fluorescent Microtubules Biochem Kit 4.2," (2012).
38. J. Hebling, G. Almasi, I. Z. Kozma, and J. Kuhl, "Velocity matching by pulse front tilting for large-area THz-pulse generation," Opt. Express **10**(21), 1161–1166 (2002).
39. H. Hirori, A. Doi, F. Blanchard, and K. Tanaka, "Single-cycle terahertz pulses with amplitudes exceeding 1 MV/cm generated by optical rectification in LiNbO3," Appl. Phys. Lett. **98**(9), 091106 (2011).
40. J. E. Bertie and Z. Lan, "Infrared intensities of liquids XX: the intensity of the OH stretching band of liquid water revisited, and the best current values of the optical constants of H20(l) at 25C between 15,000 and 1 cm-1," Appl. Spectrosc. **50**(8), 1047–1057 (1996).
41. T. Tachizaki, R. Salagicjo, S. Terada, K.-I. Kamei, and H. Hirori, "Terahertz pulse-altered gene networks in human induced pluripotent stem cells," Opt. Lett. **45**(21), 6078–6081 (2020).
42. D. R. Dalzell, J. McQuade, R. Vincelette, B. Ibey, J. Payne, R. Thomas, W. P. Roach, C. L. Roth, and G. J. Wilmink, "Damage thresholds for terahertz radiation," in *Proceedings of SPIE: Optical Interactions with Tissues and Cells XI*, San Francisco, California (2010).
43. I. Echchgadda, J. E. Grundt, C. Z. Cerna, C. C. Roth, J. A. Payne, B. L. Ibey, and G. J. Wilmink, "Terahertz radiation: a non-contact tool for selective stimulation of biological responses in human cells," IEEE Trans. Terahertz Sci. Technol. **6**(1), 54–68 (2016).
44. T. T. L. Kristensen, W. Withayachumnankul, P. U. Jepsen, and D. Abbott, "Modeling terahertz heating effects on water," Opt. Express **18**(5), 4727–4739 (2010).
45. M. Tsubouchi, H. Hoshina, M. Nagai, and G. Isoyama, "Plane photoacoustic wave generation in liquid water using irradiation of terahertz pulses," Sci. Rep. **10**(1), 18537 (2020).
46. C. M. Hough, D. N. Purschke, C. Huang, L. V. Titova, O. V. Kovalchuk, B. J. Warkentin, and F. A. Hegmann, "Intense terahertz pulses inhibit Ras signaling and other cancer-associated signaling pathways in human skin models," JPhys Photonics **3**(3), 034004 (2021).
47. A. Ben-Ze'ev, S. R. Farmer, and S. Penman, "Mechanisms of regulating tubulin synthesis in cultured mammalian cells," Cell **17**(2), 319–325 (1979).
48. T. J. Yen, P. S. Machlin, and D. W. Cleveland, "Autoregulated instability of beta-tubulin mRNAs by recognition of the nascent amino terminus of beta-tubulin," Nature **334**(6183), 580–585 (1988).
49. D. W. Cleveland, "Autoregulated control of tubulin sythesis in animal cells," Current Opinions in Cell Biology **1**(1), 10–14 (1989).
50. I. Gasic, S. A. Boswell, and T. J. Mitchison, "Tubulin mRNA stability is sensitive to change in microtubule dynamics caused by multiple physiological and toxic cues," PLoS Biol. **17**(4), e3000225 (2019).
51. G. Stelzer, N. Rosen, I. Plaschkes, S. Zimmerman, M. Twik, S. Fishilevich, T. I. Stein, R. Nudel, I. Lieder, Y. Mazor, S. Kaplan, D. Dahary, D. Warshawsky, Y. Guan-Golan, A. Kohn, N. Rappaport, M. Safran, and D. Lancet, "The GeneCards Suite: from gene data mining to disease genome sequence analysis," Current Protocols in Bioinformatics **54**(1), 1.30.1 (2016).
52. P. P. Gan, J. A. McCarroll, S. T. Po'uha, K. Kamath, M. A. Jordan, and M. Kavallaris, "Microtubule dynamics, mitotic arrest, and apoptosis: drug-induced differential effects of BIII-tubulin," Mol. Cancer Ther. **9**(5), 1339–1348 (2010).
53. P. P. Gan and M. Kavallaris, "Tubulin-targeted drug action: functional significance of Class II and class IVb B-tubulin in vinca alkaloid sensitivity," Cancer Res. **68**(23), 9817–9824 (2008).
54. S. Carbon, A. Ireland, C. J. Mungall, S. Shu, B. Marshall, and S. Lewis, "AmiGO: Online access to ontology and annotation data," Bioinformatics **25**(2), 288–289 (2009).
55. G. Orr, P. Verdier-Pinard, H. McDaid, and S. Horwitz, "Mechanisms of Taxol resistance related to microtubules," Oncogene **22**(47), 7280–7295 (2003).
56. S. Punganuru, H. Madala, and K. Srivenugopal, "Colchicine-based hybrid anticancer drugs to combat tumor heterogeneity," Med. Chem. **6**(3), 1000341 (2016).
57. M. Jordan and L. Wilson, "Microtubules as a target for anticancer drugs," Nat. Rev. Cancer **4**(4), 253–265 (2004).